

Characterization of coherent structures in three-dimensional turbulent flows using the finite-size Lyapunov exponent

João H Bettencourt, Cristóbal López and Emilio Hernández-García

IFISC (CSIC-UIB), Instituto de Física Interdisciplinar y Sistemas Complejos
Campus Universitat de les Illes Balears
E-07122 Palma de Mallorca, Spain
E-mail: joaob@ifisc.uib-csic.es

Abstract.

In this paper we use the finite size Lyapunov Exponent (FSLE) to characterize Lagrangian coherent structures in three-dimensional (3d) turbulent flows. Lagrangian coherent structures act as the organizers of transport in fluid flows and are crucial to understand their stirring and mixing properties. Generalized maxima (ridges) of the FSLE fields are used to locate these coherent structures.

Three-dimensional FSLE fields are calculated in two phenomenologically distinct turbulent flows: a wall-bounded flow (channel flow) and a regional oceanic flow obtained by numerical solution of the primitive equations where two-dimensional turbulence dominates.

In the channel flow, autocorrelations of the FSLE field show that the structure is substantially different from the near wall to the mid-channel region and relates well to the more widely studied Eulerian coherent structure of the turbulent channel flow. The ridges of the FSLE field have complex shapes due to the 3d character of the turbulent fluctuations.

In the oceanic flow, strong horizontal stirring is present and the flow regime is similar to that of 2d turbulence where the domain is populated by coherent eddies that interact strongly. This in turn results in the presence of high FSLE lines throughout the domain leading to strong non-local mixing. The ridges of the FSLE field are quasi-vertical surfaces, indicating that the horizontal dynamics dominates the flow. Indeed, due to rotation and stratification, vertical motions in the ocean are much less intense than horizontal ones. This suppression is absent in the channel flow, as the 3d character of the FSLE ridges shows.

1. Introduction

Turbulent flow occurs in the natural environmental and in technological applications with such frequency that it could be considered the "natural" state of fluid flows to be found around us. Traditionally, fluid flows have been observed and studied in the Eulerian perspective where a fixed position is observed for a definite interval of time. The other perspective, the Lagrangian, follows the motion of the fluid and thus is better suited to study aspects of fluid flow such as material transport or the deformation of fluid material in a given state of motion.

The use of stretching quantifiers such as the Lyapunov exponents, which measure the relative separation between particles [1, 2, 3, 4], has broadly improved the Lagrangian study of fluid flows. On the one hand Lyapunov methods provide information on time scales for dispersion processes, with its relevance for mixing and stirring of fluids [1, 2, 3, 5, 6, 7]. On the other, they are useful to detect the so-called Lagrangian coherent structures (LCS). LCSs [8, 9] are templates for particle advection in complex flows, separating regions with different dynamical behavior and acting as barriers and avenues to transport, fronts or eddy boundaries [9, 3, 4, 10, 6, 11, 12, 13].

Relationships of LCSs with Lyapunov fields have been established for the case of finite-time Lyapunov exponents (FTLEs) [14, 15]. These relationships state that LCS can be identified with the ridges (generalized maxima) of the FTLE field. Furthermore they state that the flux through the LCS is inversely proportional to the strength of the ridge and to the integration time of the FTLE field calculation. This flux is shown to be small and the LCS extracted as the ridges of FTLE fields are considered to be almost material-like surfaces. This identification has become widely used in the field although it should be mentioned that there are other more precise definitions of LCS [11, 16, 17], that consider LCS to be exact material surfaces admitting zero flux across them. In our work, we use instead finite-size Lyapunov exponents (FSLEs), which quantify the separation rate of fluid particles between two given distance thresholds [1, 2]. They turn out to be convenient for the case of bounded flows in which characteristic spatial scales are more direct to identify than temporal ones and have been shown to be robust with respect to noisy or poorly resolved velocity fields [18]. Although a rigorous connection between the FSLE and LCSs has not been established yet, previous work [10, 6, 19, 12, 20] has shown that the ridges of the FSLE behave in a similar fashion as the ridges of the FTLE field. Following these works we assume that LCSs can be computed as ridges of FSLEs, and that they are transported by the flow as almost material surfaces/lines, with negligible flux of particles through them. Observations presented here are consistent with those assumptions.

Despite its relevance in real flows, the full three-dimensional (3d) structure of LCSs is still an open subject. In 3d flows, LCS were explored in atmospheric contexts [21, 22, 23], and in a turbulent channel flow at $Re_\tau = 180$ in [24]. A kinematic ABC flow was studied in [25]. In the ocean, where it is widely recognized that filamental structures, eddies, and in general oceanic meso- and submeso-scale structures have a great influence

on marine ecosystems [26, 27, 28, 29], the identification of LCSs and the study of their role in the transport of biogeochemical tracers has primarily been restricted to two-dimensional (2d) layers [30, 31, 32, 33]. There are two concurrent reasons for this: a) because of stratification and rotation, vertical motions in the ocean are usually very small when compared to horizontal displacements; b) synoptic measurements (e.g. from satellites) of relevant quantities are restricted to the surface. A few previous results for Lagrangian eddies in 3d were obtained in Refs. [34, 35], by applying the methodology of lobe dynamics and the turnstile mechanism. Also, Refs. [36, 37] used 3d FSLE fields to identify LCS in oceanic flows. In particular, a mesoscale eddy in the Southern Atlantic was studied in [37], and it was shown that oceanic LCSs presented a vertical curtain-like shape, i.e. they look mostly like vertical sheets, and that material transport into and out of the mesoscale eddy occurred through filamentary deformation of such structures.

In this paper, we use 3d fields of FSLE to identify LCSs in a turbulent channel flow and in an oceanic flow. Observations of the similarities and differences between the two systems, both in their computation and their physical meaning, helps to appreciate the power and scope of this Lagrangian technique in the analysis of fluid flows. In Section 2 we describe the methodology used to identify LCSs in 3d turbulent flows. Sections 3 and 4 are devoted to the turbulent channel flow and the oceanic flow, respectively, and Section 5 presents our conclusions and directions for future work.

2. Methods

2.1. Finite-Size Lyapunov Exponents.

In order to study non-asymptotic dispersion processes such as stretching at finite scales and bounded domains, the finite size Lyapunov Exponent was introduced [1, 2, 3]. It is defined as:

$$\lambda = \frac{1}{\tau} \log \frac{d_f}{d_0}, \quad (1)$$

where τ is the time it takes for the separation between two particles, initially d_0 , to reach a value d_f . In addition to the dependence on the values of d_0 and d_f , the FSLE depends also on the initial position of the particles and on the time of deployment. Locations (i.e. initial positions) leading to high values of this Lyapunov field identify regions of strong separation between particles, i.e., regions that will exhibit strong stretching during evolution, that can be identified with the LCS [3, 10, 6].

In principle, to compute FSLE in 3d, the method of [6] can be extended to include the third dimension, by computing the time it takes for particles initially separated by $d_0 = [(\Delta x_0)^2 + (\Delta y_0)^2 + (\Delta z_0)^2]^{1/2}$ to reach a final distance of $d_f = [(\Delta x_f)^2 + (\Delta y_f)^2 + (\Delta z_f)^2]^{1/2}$. We will proceed this way for the turbulent channel, but, as indicated in [37], vertical displacements are much smaller than horizontal ones in ocean flows. Therefore, the displacement in the z direction does not contribute significantly to the calculation of d_f in the ocean, which prompt us to implement a quasi-3d computation of FSLEs: we use the full 3d velocity field for particle advection

81 but particles are initialized in 2d horizontal ocean layers and the contribution Δz_f is
 82 not considered when computing d_f (see more details in [37]). In any case, since we allow
 83 the full 3d trajectories of particles, we take into account the vertical dynamics of the
 84 oceanic flows.

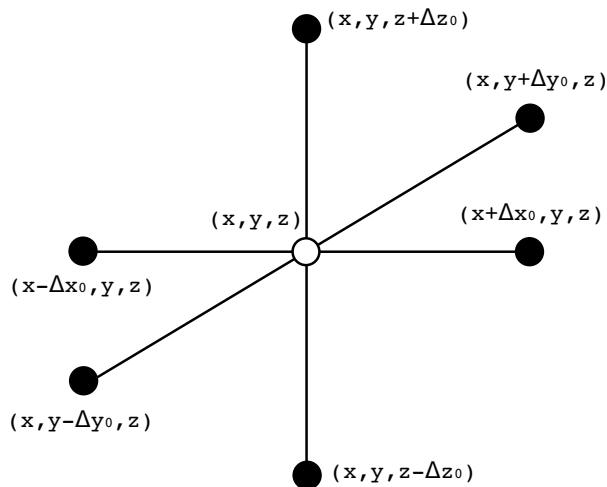


Figure 1. Computational setup for the calculation of the FSLE field in 3d. The FSLE at the location of the central particle (\circ) is a measure of the time it takes for any of the neighbor particles (\bullet) to diverge from the central particle by a distance greater than δ_f .

85 Concerning the turbulent channel, where we can implement a fully 3d computation
 86 of the FSLE, we proceed as follows. A grid of initial locations $\mathbf{x}_0 = (x_i, y_j, z_k)$ is set
 87 up at time t , fixing the spatial resolution of the FSLE field (figure 1). Particles are
 88 released from each grid point and their three-dimensional trajectories are calculated.
 89 The distances of each neighbor particle with respect to the central one (initially d_0) is
 90 monitored until one of the separations reaches a value d_f .

91 In both systems considered, we obtain two different types of FSLE maps by
 92 integrating the three-dimensional particle trajectories backward and forward in time:
 93 the attracting LCSs (for the backward), and the repelling LCSs (forward) [10, 6]. We
 94 obtain in this way FSLE fields with a spatial resolution given by d_0 . When a particle
 95 leaves the velocity field domain or reaches a no-slip boundary, the FSLE value at its
 96 initial position and initial time is set to zero. If the interparticle separation remains
 97 smaller than d_f past a maximum integration time Δt , then the FSLE for that location
 98 is also set to zero.

99 2.2. Lagrangian Coherent Structures.

100 The identification of LCS calculated from Lyapunov fields in 2d flows is straightforward
 101 since they practically coincide with (finite-time) stable and unstable manifolds of
 102 relevant hyperbolic structures in the flow [8, 9, 10] (but see [38, 16]). The structure

103 of these manifolds in 3d is generally much more complex than in 2d [25, 39], and they
 104 can be locally either lines or surfaces.

105 Differently than 2d, where LCS can be visually identified as the maxima of the
 106 FSLE field, in 3d they are hidden within the volume data and one needs to explicitly
 107 compute and extract them, using the definition of LCSs as the ridges of the FSLE field.
 108 A ridge L is a co-dimension 1 orientable, differentiable manifold (which means that for
 109 a 3d domain D , ridges are surfaces) satisfying the following conditions [15]:

- 110 (i) The field λ attains a local extremum at L .
- 111 (ii) The direction perpendicular to the ridge is the direction of fastest descent of λ at
 112 L .

113 The method used to extract the ridges from the scalar field $\lambda(\mathbf{x}_0, t)$ is from [40]. It
 114 uses an earlier [41] definition of ridge in the context of image analysis, as a generalized
 115 local maxima of scalar fields. For a scalar field $f : \mathbb{R}^n \rightarrow \mathbb{R}$ with gradient $\mathbf{g} = \nabla f$ and
 116 Hessian \mathbf{H} , a d -dimensional height ridge is given by the conditions

$$117 \quad \forall d < i \leq n, \quad \mathbf{g}^T \mathbf{e}_i = 0 \text{ and } \alpha_i < 0, \quad (2)$$

118 where $\alpha_i, i \in \{1, 2, \dots, n\}$, are the eigenvalues of \mathbf{H} , ordered such that $\alpha_1 \geq \dots \geq$
 119 α_n , and \mathbf{e}_i is the eigenvector of \mathbf{H} associated with α_i . For $n = 3$, Eq. (2) becomes

$$120 \quad \mathbf{g}^T \mathbf{e}_3 = 0 \text{ and } \alpha_3 < 0. \quad (3)$$

121 In other words, in \mathbb{R}^3 the $\mathbf{e}_1, \mathbf{e}_2$ eigenvectors point locally along the ridge and the
 122 \mathbf{e}_3 eigenvector is orthogonal to it, so the ridge maximizes the scalar field in the normal
 123 direction to it and in this direction the field is more convex than in any other direction,
 124 since the eigenvector associated with the most negative eigenvalue is oriented along the
 125 direction of maximum negative curvature of the scalar field.

126 The extraction process progresses by calculating the points where the ridge
 127 conditions are verified and the ridge strength $|\alpha_3|$ is higher than a predefined threshold
 128 s so that ridge points whose value of α_3 is lower (in absolute value) than s are discarded
 129 from the extraction process. Since the ridges are constructed by triangulations of the set
 130 of extracted ridge points, the strength threshold greatly determines the size and shape
 131 of the extracted ridge, by filtering out regions of the ridge that have low strength. The
 132 reader is referred to [40] for details about the ridge extraction method. The height ridge
 133 definition has been used to extract LCS from FTLE fields in several works (see, among
 134 others, [42]).

135 Since the λ value of a point on the ridge and the ridge strength α_3 are only related
 136 through the expressions (2) and (3), the relationship between the two quantities is not
 137 direct, which makes difficult to choose the appropriate strength threshold s . A too
 138 small value of s will result in the extraction of very small LCSs that appear to have
 139 little influence on the dynamics, while a large value will result in only a partial rendering
 140 of the larger and more significant LCS, limiting the possibility of observing their real
 141 impact on the flow.

142 The ridges extracted from the backward FSLE map approximate the attracting
 143 LCSs, and the ridges extracted from the forward FSLE map approximate the repelling
 144 LCSs. The attracting ones are the more interesting from a physical point of view [6, 12],
 145 since particles (or any passive scalar driven by the flow) typically approach them and
 146 spread along them, so that they are good candidates to be identified with the typical
 147 filamentary structures observed in tracer advection.

148 3. Turbulent channel flow

149 Turbulent channel flow is a turbulent flow between two stationary, parallel walls
 150 separated by a distance 2δ . It has been studied extensively due to its geometrical
 151 simplicity and its wall-bounded nature, which makes it a suitable platform to
 152 study phenomena appearing in more complex turbulent wall-bounded flows of great
 153 technological interest.

154 The coordinates of the flow are: x for the streamwise direction, y for the cross-
 155 stream coordinate that separates the two plates, and z for the spanwise direction. The
 156 flow is maintained by a downstream pressure gradient $\frac{dP_0}{dx}$ acting against the wall shear
 157 stress. The laminar flow solution U_0 is a cross-stream parabolic profile given by

$$158 \quad U_0(y) = \frac{y^2 - \delta^2}{2\mu} \frac{dP_0}{dx}, \quad (4)$$

159 where μ is the dynamic viscosity. Following the Reynolds averaging method [43], the
 160 turbulent flow velocity \mathbf{u} is decomposed in a mean $\mathbf{U} = (U(y), 0, 0)$ and a fluctuating
 161 component $\mathbf{u}' = (u', v', w')$. The mean turbulent velocity profile $U(y)$ differs from the
 162 laminar one, $U_0(y)$, by a lower centerline velocity $U(0)$ and increased near-wall velocity
 163 giving it a flatter shape. Due to the increase in mean velocity near the wall, the shear
 164 stress near the wall is higher for the turbulent case. The total shear stress τ appearing
 165 in the averaged Reynolds equations gets contributions from both the viscous stress and
 166 the Reynolds stress $-\overline{u'v'}$ associated to the velocity fluctuations:

$$167 \quad \frac{\tau}{\rho} = \nu \frac{dU}{dy} - \overline{u'v'} \quad (5)$$

168 $\nu = \mu/\rho$ is the kinematic viscosity. The symmetries of the domain and the Reynolds
 169 equations imply that τ depends only on the cross-stream coordinate y , and the
 170 dependence is linear, so that it can be written as

$$171 \quad \frac{\tau(y)}{\rho} = u_\tau^2 \left(1 - \frac{y}{\delta}\right) \quad (6)$$

172 The shear velocity u_τ gives the velocity scale of the turbulent velocity fluctuations. The
 173 formula [43]:

$$174 \quad \rho u_\tau^2 = \mu \left. \frac{dU(y)}{dy} \right|_{y=0} \quad (7)$$

175 allows to compute u_τ from measurements of the mean velocity profile from the
 176 simulations. A length scale can be formed by combining u_τ with ν : the wall scale

177 $\delta^+ = \nu/u_\tau$. The wall distance can now be expressed as $y^+ = y/\delta^+$, and the same
 178 normalization could be done for the rest of coordinates. The viscous Reynolds number
 179 $Re_\tau = \delta/\delta^+$ is simply the ratio between the two relevant length scales.

180 The existence of coherent structures in turbulent wall-bounded flows has been
 181 known for several decades from investigations on intermittency in the interface between
 182 turbulent and potential flow regions, on the large eddy motions in the outer regions of
 183 the boundary layer, and on coherent features in the near-wall region ([44] and references
 184 therein). Since then, through experimental and numerical investigations, a picture of the
 185 organization of these coherent structures in the turbulent boundary layer has emerged,
 186 which has become rather complete from the Eulerian point of view [44, 45]. Our
 187 approach is a contribution to the Lagrangian exploration of these coherent structures,
 188 as in [24] and [46].

189 The longitudinal velocity field in the inner region of the channel (the viscous
 190 sublayer adjacent to the wall and the intermediate buffer region) is organized into
 191 alternating streamwise streaks of high and low speed fluid. Turbulence production
 192 occurs mainly in the buffer region in association with intermittent and violent outward
 193 ejections of low-speed fluid and inrushes of high-speed fluid towards the wall. The outer
 194 region is characterized by the existence of three-dimensional δ -scale bulges that form on
 195 the turbulent/potential flows interface. Irrotational valleys appear at the edges of the
 196 bulges, entraining high-speed fluid into the turbulent inner region. A central element in
 197 the structure of the turbulent boundary layer is the hairpin vortex, mainly because it
 198 is a structure with the capability of transporting mass and momentum across the mean
 199 velocity gradient and because it provides a paradigm with which to explain several
 200 observations of wall turbulence [44, 47].

201 3.1. Data

202 The data used to extract the LCS come from a direct numerical simulation (DNS) of
 203 turbulent channel flow at a viscous Reynolds number $Re_\tau = 180$. The setup of the
 204 simulation follows that of [48] and is summarized in table 1. The simulations were
 205 conducted using the CFD solver `Channelflow.org` [49]. The `Channelflow.org` code
 206 solves the incompressible Navier-Stokes equations in a rectangular box with dimensions
 207 $L_x \times 2\delta \times L_z$, with periodic boundary conditions in the x (so that fluid leaving the
 208 computational domain in the direction of the mean flow at $x = L_x$ reenters it at $x = 0$)
 209 and in the spanwise z direction. No-slip conditions are imposed on $y = \pm\delta$. The
 210 unsteady velocity field \mathbf{u} is represented as a combination of Fourier modes in the x and
 211 z directions and of Chebyshev polynomials in the wall-normal direction. The pressure
 212 gradient necessary to balance the friction at the walls was chosen as to maintain a
 213 constant bulk velocity of $\frac{2}{3}U_0$. Time stepping is a 3rd-order Semi-implicit Backward
 214 Differentiation. Note that in our computations $\delta^+ = 1/Re_\tau = 0.0058$ so that in wall
 215 units $0 < y^+ < 344$.

216 The flow was integrated from an initial base-flow with parabolic profile and a

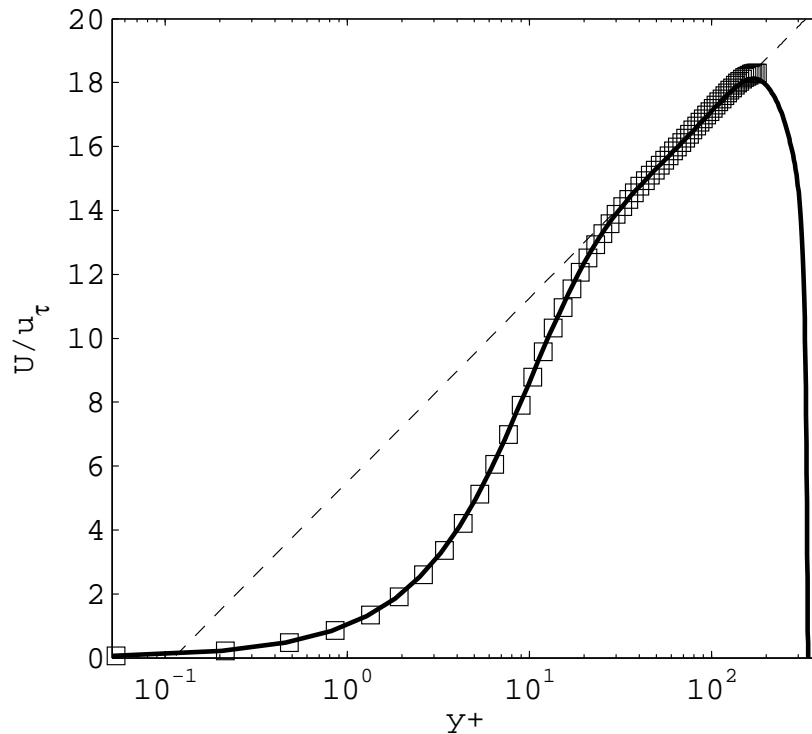


Figure 2. Mean velocity profile $U(y)/u_\tau$. Solid line: our simulations; squares: [48]; dashed line: logarithmic profile $U(y)/u_\tau = 2.5 \log(y^+) + 5.5$.

217 small disturbance that evolved into a fully developed turbulent flow. The total
 218 integration time was $\Delta t = 600$ time units that in dimensionless form $t^+ = t(u_\tau^2/\nu)$
 219 gives $\Delta t^+ = 83.54$. After an initial transient of about 200 time units the simulations
 220 reached a statistically stationary state from which statistics was accumulated.

221 The mean quantities and first order statistics of our simulations where compared
 222 to those of [48] and the agreement is quite good. The profile of the mean velocity in
 223 wall units is shown in figure 2. The profile for the Reynolds stress $-\overline{u'v'}$ shows that the
 224 maximum (in absolute value) is located at approximately $y^+ = 30$, in the outer limit of
 225 the buffer layer (see figure 3).

226 3.2. Results

227 The LCS were extracted from the turbulent velocity field data described in the previous
 228 section. A calculation of FSLE field in the entire turbulent channel was conducted in
 229 order to understand the statistical properties of the FSLE field in this class of turbulent
 230 flows. A subsequent calculation in a subdomain of the channel was used to extract the
 231 LCS in that subdomain for a sequence of time instants. The setup of both calculations
 232 is shown in table 2.

233 3.2.1. *The 3d FSLE field.* The 3d backward FSLE field for the entire channel was
 234 calculated at a single time instant in the statistically steady state. The initial and final

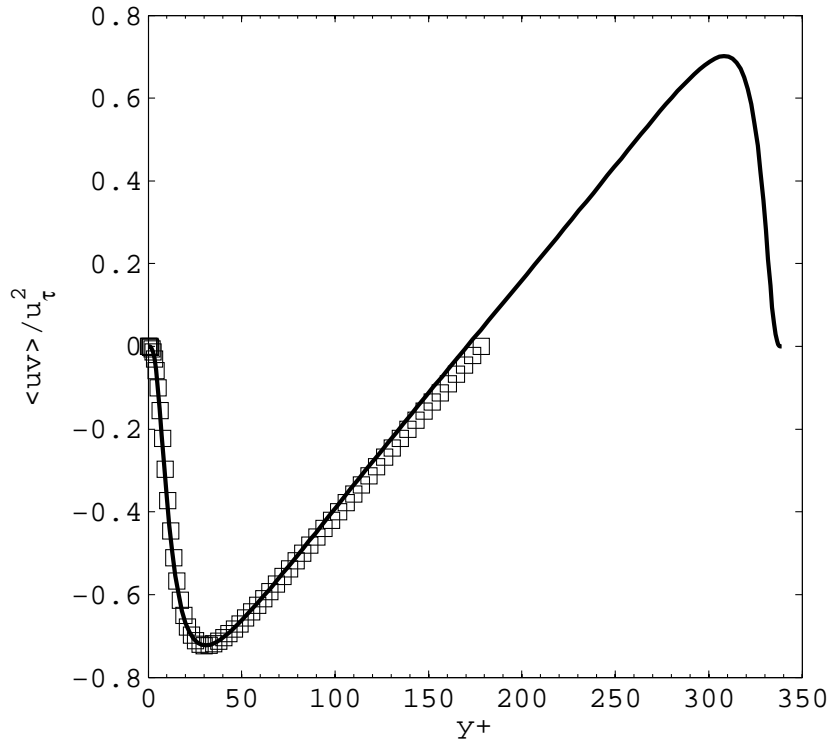


Figure 3. Reynolds stress $\overline{u'v'}$ profile at $Re_\tau = 180$. Solid line: our simulations; squares: [48] (given up to the channel centerline).

Table 1. Simulation parameters. Quantities with $^+$ refer to wall units. L_x , 2δ and L_z are the domain sizes in the x , y and z directions. Δx^+ , Δy^+ and Δz^+ are the respective spatial resolutions (given at the first point above the wall for the y case), and n_x , n_y and n_z the corresponding number of grid points. $Re = U\delta/\nu$ is the Reynolds number based on the channel center mean speed, whereas $Re_\tau = u_\tau\delta/\nu$ is the viscous Reynolds number. The nominal value is an input to the computer code, and the actual value comes by using Eq. (7) for the computed mean profile $U(y)$.

Re channel center	4000	Re_τ nominal	180	Re_τ actual	172
L_x	4π	δ	1	L_z	$\frac{4}{3}\pi$
L_x^+	2166.61	δ^+	0.0058	L_z^+	722.20
n_x	128	n_y	129	n_z	128
Δx^+	17.06	Δy^+	0.005	Δz^+	5.6867

Table 2. FSLE calculation parameters. dt is the integration time step and Δt the maximum integration time.

Calculation	d_0	d_f/d_0	Δt	dt
Complete channel	0.024	20	20	0.05
LCS subdomain	0.003	67	10	0.05

235 distances d_0 and d_f were chosen as a balance between encompassing the widest possible
 236 range of scales of motion (measured by the ratio d_f/d_0), and adequate resolution and
 237 computational cost. The initial distance is of the order of $4\delta^+$ and the final distance of
 238 the order of 0.5δ – a typical scale of coherent structures found in the turbulent channel
 239 flow – so that the ratio of scales, d_f/d_0 , is approximately $Re_\tau/8$.

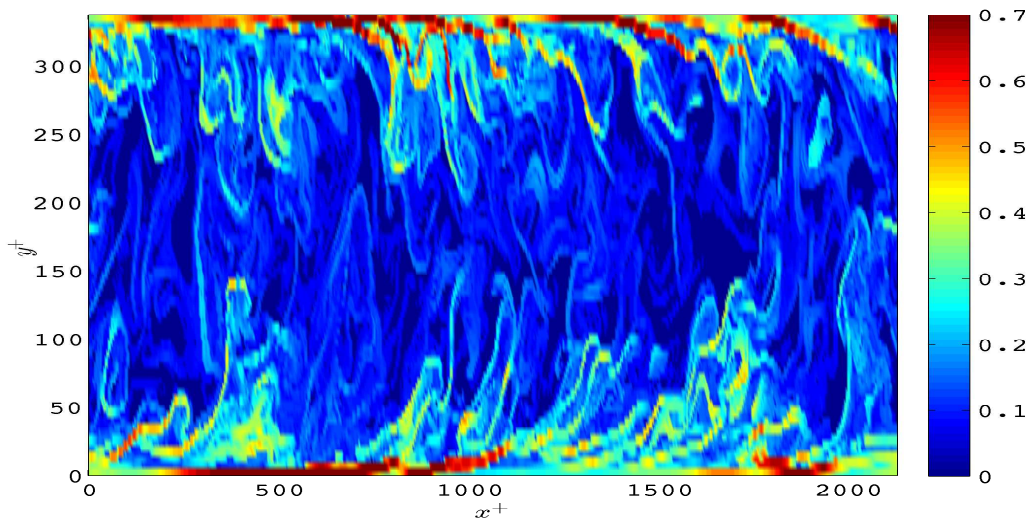


Figure 4. Instantaneous FSLE field at $t = 420$ shown on a streamwise/wall-normal plane in the turbulent channel. Walls are at the top and bottom of the figure. Mean velocity is in the streamwise direction from left to right.

240 Figure 4 shows an instantaneous configuration of the FSLE values in a
 241 streamwise/wall-normal plane. The maxima of the FSLE appear to be located close
 242 to the walls with occasional sloping structures extending to the midchannel region. The
 243 channel center is devoid of high FSLE values but coherent patches of low FSLE values
 244 can still be observed. These structures are not distributed uniformly along the length of
 245 the channel but appear to be organized in packets. This organization bears resemblance
 246 to the widely accepted picture of organized structures in wall turbulence where the outer
 247 region is dominated by packets of sloping hairpin vortices and the inner region by near
 248 wall vortices (the hairpin vortices legs) and shear layers [47, 44].

249 A cross-stream FSLE profile is obtained by averaging the 3d field over the periodic
 250 directions x and z . It is shown in figure 5. The profile is symmetric about the channel
 251 centerline and shows a maximum at approximately $y^+ = 4$, inside the viscous sublayer
 252 (this location corresponds to the first grid point off the wall).

253 Because of the periodic boundary conditions in the x and z directions the
 254 average profiles along these directions are rather unstructured, and we resort to
 255 two-point correlation functions to quantify the statistical structure properties. For
 256 each plane parallel to the walls, i.e. for each value of y^+ , we compute the
 257 fluctuations of the FSLE values around the average in that plane: $\Lambda(x^+, y^+, z^+) \equiv$

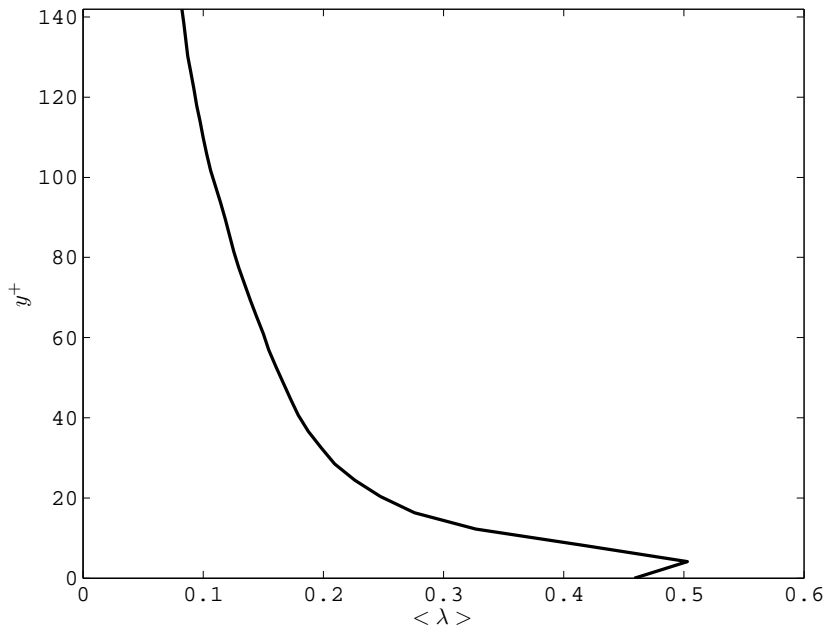


Figure 5. FSLE profile averaged over (x, z) , as a function of the cross-stream normalized coordinate y^+ . Only half of the channel is shown since the profile is quasi-symmetric about the channel centerline.

258 $\lambda(x^+, y^+, z^+) - \langle \lambda(x^+, y^+, z^+) \rangle_{x^+, z^+}$. From this quantity we define the streamwise
 259 $R_{xx}(y^+; \bar{x}^+)$ correlation function as:

$$260 \quad R_{xx}(y^+; \bar{x}^+) = \frac{\langle \Lambda(x^+, y^+, z^+) \Lambda(x^+ + \bar{x}^+, y^+, z^+) \rangle_{x^+, z^+}}{\langle \Lambda(x^+, y^+, z^+)^2 \rangle_{x^+, z^+}}, \quad (8)$$

261 and the spanwise $R_{zz}(y^+; \bar{z}^+)$ correlation function

$$262 \quad R_{zz}(y^+; \bar{z}^+) = \frac{\langle \Lambda(x^+, y^+, z^+) \Lambda(x^+, y^+, z^+ + \bar{z}^+) \rangle_{x^+, z^+}}{\langle \Lambda(x^+, y^+, z^+)^2 \rangle_{x^+, z^+}}. \quad (9)$$

263 In the above equations the averages are over the periodic directions x^+ and z^+ . The
 264 correlations are shown in Figs. 6 and 7 at different distances from the walls: one
 265 smaller, one larger, and one approximately coincident with the location of the maximum
 266 Reynolds stress. These functions reveal sizes and organization of the different structures
 267 in the Lagrangian FSLE field, to be contrasted with Eulerian correlation functions in
 268 the same system [50].

269 Close to the wall ($y^+ = 4$ and $y^+ = 12.2$), viscous effects dominate. The
 270 correlations show that the FSLE field is organized in streamwise structures of length
 271 scale approximately $l^+ \sim 500$ wall units. In the transverse direction z^+ the oscillations
 272 seen in R_{zz} for $y^+ = 4$ indicate an approximately periodic arrangement of the streaks
 273 [24], with a spacing $\sim 50 - 100$ wall units. This pattern of organization is similar to
 274 what is seen in Eulerian descriptions [50, 44].

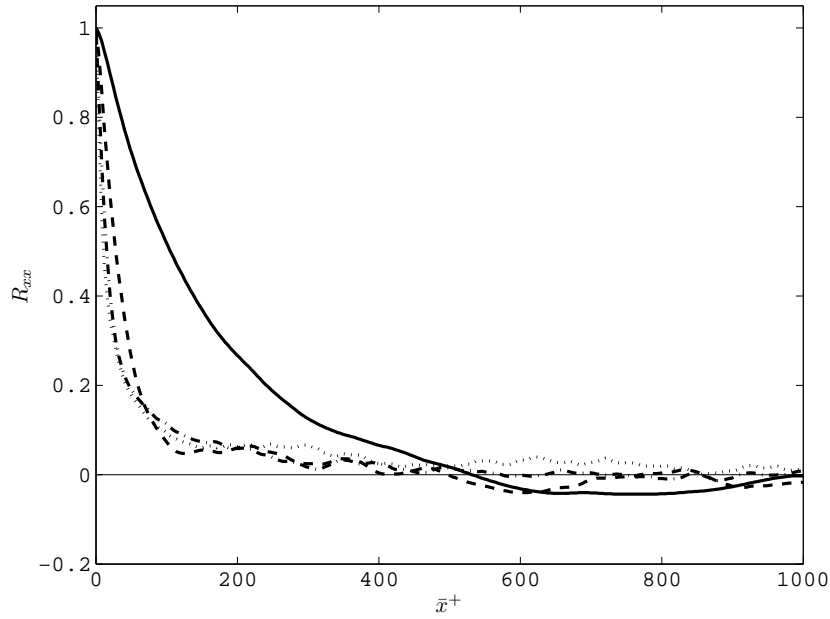


Figure 6. Streamwise correlation function $R_{xx}(y^+; \bar{x}^+)$ as a function of the streamwise separation \bar{x}^+ , at four distances from the lower wall: Continuous line: $y^+ = 4$; dashed line $y^+ = 12.2$; dash-dot line $y^+ = 28.4$; dotted line: $y^+ = 122.1$.

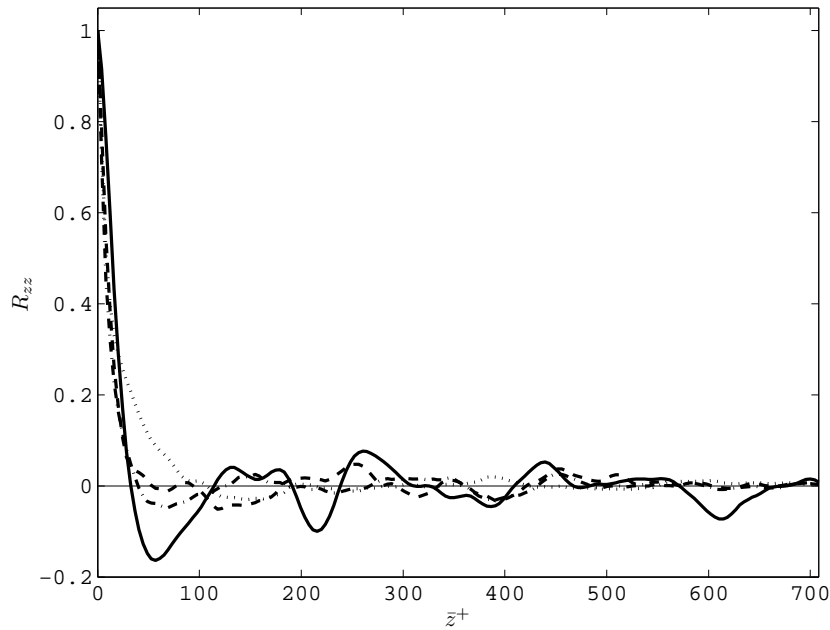


Figure 7. Spanwise correlation function $R_{zz}(y^+; \bar{z}^+)$ as a function of the spanwise separation \bar{z}^+ , at four distances from the lower wall: Continuous line: $y^+ = 4$; dashed line $y^+ = 12.2$; dash-dot line $y^+ = 28.4$; dotted line: $y^+ = 122.1$.

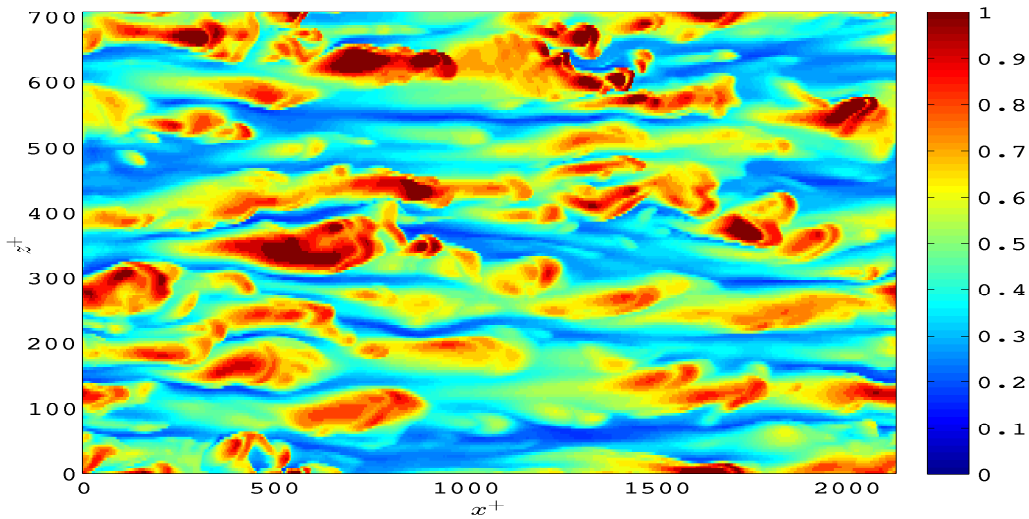


Figure 8. Instantaneous FSLE field in plane parallel to the wall at $y^+ = 4$. The time is the same as in figure 4

275 At planes further away from the wall ($y^+ = 28.4$ and $y^+ = 122.1$ in Figs. 6 and 7),
 276 correlation functions in both directions become shorter ranged, and periodic features are
 277 progressively lost. This corresponds to a rather disordered distribution of structures,
 278 each with a typical size related to the width of the correlation functions, i.e. of the order
 279 of 50 wall units, as also seen in figure 4.

280 An instantaneous near-wall FSLE field is shown in figure 8, where the high FSLE
 281 values appear in slender and elongated structures with length and width corresponding
 282 to the streamwise and spanwise correlation lengths discussed above. It is unclear whether
 283 the correlation lengths result from a single streamwise structure or from the overlapping
 284 of shorter structures (a feature of the near wall coherent structure arrangement [51]).

285 These are the highest FSLE values that are to be found in the channel as the plot
 286 in figure 5 shows. The mechanism for the formation of these structures could be the
 287 lifting of low speed fluid close to the wall by the action of counter rotating vortex pairs
 288 located above the viscous sublayer (see figure 9). This mechanism is widely known in
 289 the Eulerian view of coherent structures of turbulent wall bounded flows (*ejections* or
 290 *bursting*, [47]).

291 The near wall fluid is advected away from the wall by the action of these vortices.
 292 This mechanism could be responsible for very fast particle separation in particle pairs
 293 where one particle is lifted away and the other remains in the low speed zone close to the
 294 wall. We note that the particle separation would increase not only by the wall normal
 295 distance between particles but also because the ejected particle would move to a region
 296 with higher streamwise velocity. Shear layers near the wall is another possible way to
 297 produce large particle dispersion. These mechanisms would explain the fact that the
 298 maximum average FSLE is located so close to the wall and not on the buffer region where

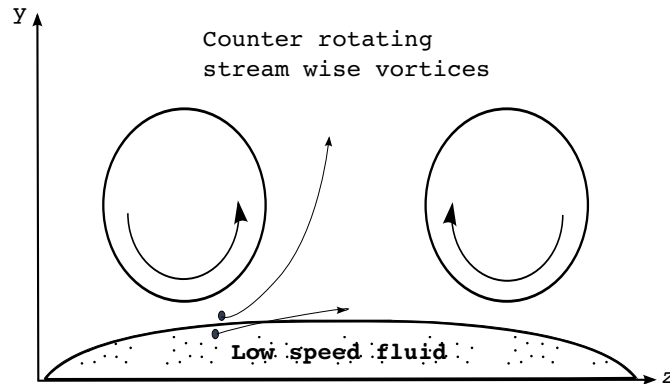


Figure 9. Mechanism for the rapid separation of fluid from the near wall viscous sublayer. The mean flow is into the page.

299 turbulence production is larger. To conclude, we note that these high FSLE regions near
 300 the wall seem to extend to the midchannel region in an inclined fashion. It is not clear
 301 whether this pattern signals the existence of a hairpin vortex with streamwise legs and
 302 inclined head or if there are two separate structures: the streamwise vortices *and* the
 303 hairpin arch or head [44]. Also, we note that the interpretation of the high FSLE regions
 304 near the wall do not require the existence of a counter rotation pair of vortices, as only
 305 one vortex would suffice.

306 To illustrate these mechanisms, a map of the FSLE field in a spanwise/wall normal
 307 plane for the LCS domain calculation is shown in figure 10, together with a set of
 308 passive particles initially located in a rectangular region close to the wall and released
 309 some instants before the time of the FSLE map. In order to focus just on the above
 310 mentioned ejection mechanism involving only the vertical motion of the particles, the
 311 trajectory integration was made in a 2d fashion by setting the longitudinal component
 312 of the particles velocity to zero.

313 The particles seem to have been lifted from wall by a streamwise vortex located
 314 to the left of the particle plume, with center at $(z^+, y^+) \sim (340, 30)$. We note that
 315 the structures are moving with the mean flow and that the continuous motion of the
 316 particles away from the wall is due to the passage of a streamwise structure that imparts
 317 this sustained motion to the particles for long enough time. To compare the Eulerian
 318 and Lagrangian coherent structures, figure 11 shows the turbulent velocity components
 319 in the same plane at the nearest time available in the turbulent dataset. The signature
 320 of the streamwise vortex discussed above can be seen in the Eulerian map at the same
 321 location. It is embedded in a patch of negative streamwise velocity fluctuation u . To
 322 the right, close to $z^+ = 380$, a vertical shear layer appears dividing the negative and
 323 positive patches of u . The Lagrangian signature of this vertical shear layer is not very
 324 strong and appears in figure 10 as quasi-vertical line of moderate FSLE extending from

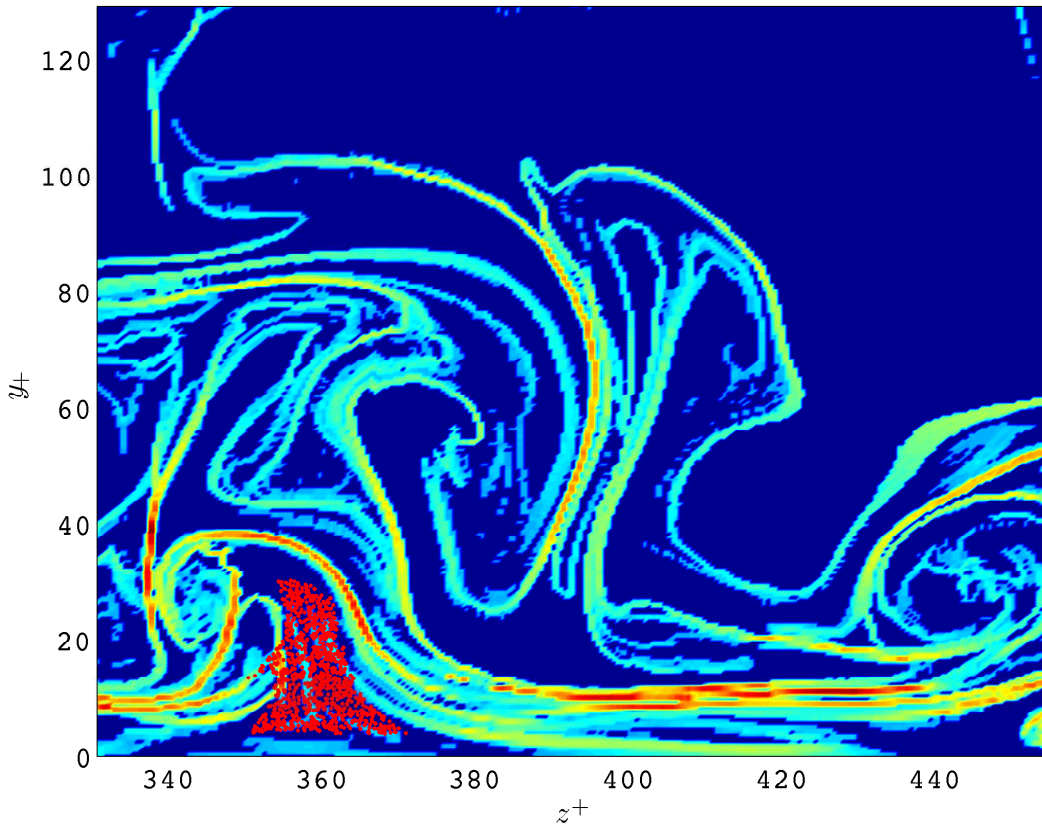


Figure 10. FSLE map in a (z, y) plane located at $x = 6.0$ ($x^+ = 1034$). The time of the map is $t = 413.8$. together with a set of particles initially located in rectangular region $z^+ \in [345, 380]$ and $y^+ \in [3.4, 13.8]$. The particles were released at $t = 409$. Particle trajectories were integrated using only the spanwise and wall normal velocity components. The mean flow is moving out of the page.

325 $y^+ = 25$ to $y^+ = 60$. On the lower right of the map, there is a set of high FSLE
 326 lines almost parallel to wall, signalling the existence of high particle dispersion. In the
 327 Eulerian map (figure 11), it can be seen that there is a shear layer parallel to the wall
 328 at the same location ($400 < z^+ < 440$ and $y^+ \sim 8$). The fact that this shear layer has
 329 a much stronger Lagrangian signature than the vertical shear layer could be because it
 330 has the same orientation and sign of the mean shear and therefore acts together with
 331 the latter to disperse neighboring particles across the wall normal direction. The high
 332 FSLE line seen at the middle of the map in figure 10, separating the two convoluted
 333 features can be seen to be related to the existence of two counter-rotating vortices, one
 334 with center located at $\sim (380, 60)$ and the other at $\sim (420, 100)$. The line of high FSLE
 335 line is seen to be located at the boundary between both vortices. In section 3.2.3, we
 336 present a 3d view of these structures and their evolution in time.

337 *3.2.2. Propagation velocity.* In turbulent channel flow the velocity perturbations
 338 propagate in the streamwise direction approximately with the velocity of the mean
 339 flow[52]. In the case of Lyapunov exponents, [46] measured the FTLE field in an 2D

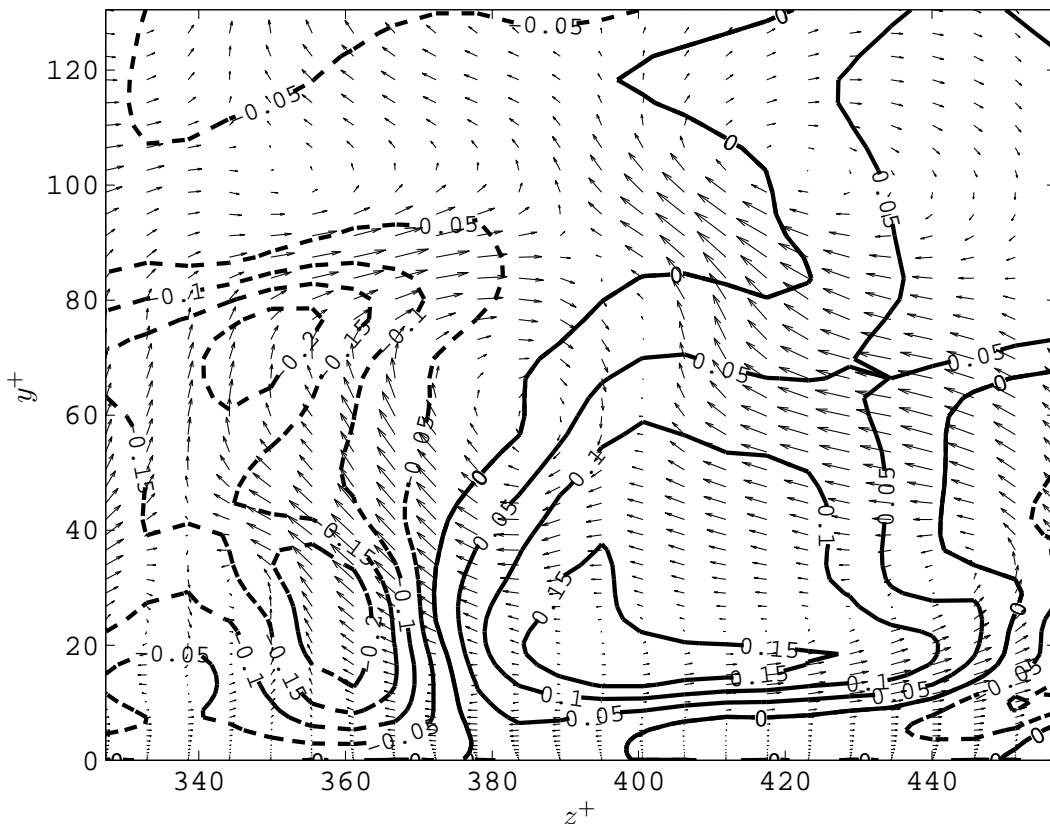


Figure 11. Instantaneous turbulent velocity components at $x = 6.0$ ($x^+ = 1034$) and $t = 413.75$. Velocity vectors correspond to the inplane velocity components (w, v) , together with contours of streamwise turbulent velocity u . Dashed contours are negative u (into the paper) and continuous contours are positive u (from the paper).

340 turbulent boundary layer velocity field obtained by time-resolved PIV measurements.
 341 The FTLE maxima were found to move with the mean flow velocity.

342 We measured the propagation velocity of the FSLE field perturbation using a space-
 343 time correlation of the form:

$$344 \quad R_{uu}(y^+; \bar{x}^+; \bar{t}^+) = \frac{\langle \Lambda(x^+, y^+, z^+, t^+) \Lambda(x^+ + \bar{x}^+, y^+, z^+, t^+ + \bar{t}^+) \rangle_{x^+, z^+}}{\langle \Lambda(x^+, y^+, z^+, t^+)^2 \rangle_{x^+, z^+}}, \quad (10)$$

345 where \bar{x}^+ and \bar{t}^+ are the delays in the streamwise direction and time. The time
 346 delay is fixed and the propagation velocity is defined as

$$347 \quad V^+ = \frac{\bar{X}^+}{\bar{t}^+}, \quad (11)$$

348 where \bar{X}^+ is the streamwise lag for which R_{uu} is maximum. The choice of the time
 349 delay is related to the time scale of the FSLE field. A first rule is to choose a time delay
 350 that gives reasonable peaks in the correlation. If there are several time scales present,
 351 several \bar{t}^+ will result in correlations exhibiting peaks. The calculation of (11) was made
 352 for a full length and height spanwise section of the channel. A time series of FSLE fields

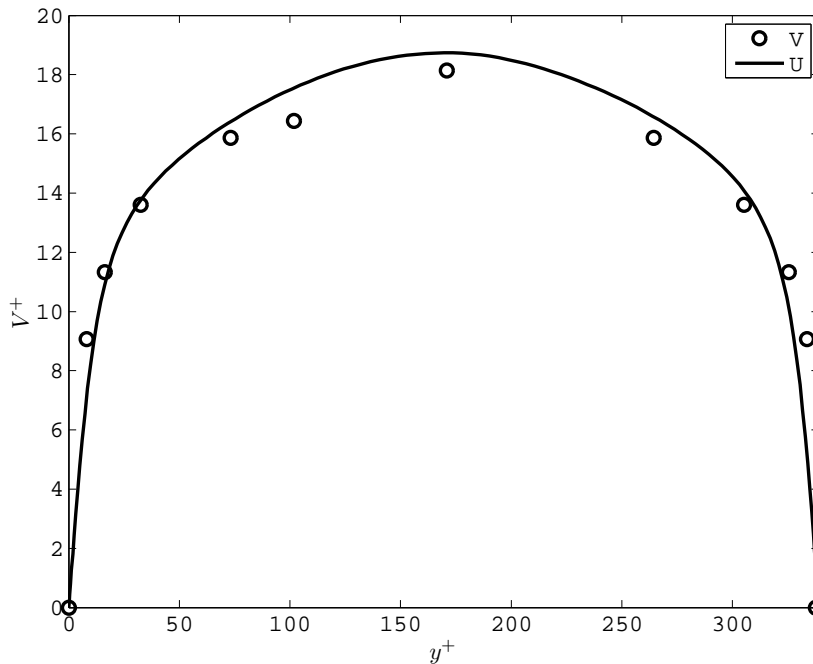


Figure 12. Propagation velocity of FSLE field (V^+) and mean flow (U^+).

353 with time step of $dt^+ = 1.8$ and time length $\Delta t^+ = 431$ was calculated for this section to
 354 offset the effects of the limited spanwise extent of the section. The final time lag used in
 355 (11) was equal to dt^+ . All larger delays produced correlations with no significant peak.
 356 A reason for this could be the fact that by setting the FSLE final distance the length
 357 scales of turbulence retained in the FSLE field is fixed, and then there will be only one
 358 time delay producing a peak in the correlation (10), specifically that corresponding to
 359 V^+ .

360 The profile of the propagation velocity is shown in figure 12. The propagation
 361 velocity is very close to the mean flow velocity. The result shows that the maxima of
 362 the FSLE field, that produce high values of R_{uu} and where we expect to find the ridges
 363 of the FSLE field, move with the flow. Hence, one may conclude, as expected, that the
 364 FSLE ridges also move with the flow approximately as material surfaces.

365 *3.2.3. The 3d LCS.* The previous description summarized the statistical properties
 366 of the different structures appearing in an instantaneous FSLE field. To make further
 367 progress we now extract three-dimensional attracting LCSs in a region of the channel
 368 at a series of time instants. The extraction domain had dimensions $L_x^+ \times L_y^+ \times L_z^+ =$
 369 $103 \times 129 \times 124$. The initial separation d_0 and distance ratio d_f/d_0 were increased from
 370 the previous calculation to improve the resolution and extract smoother structures, but
 371 sacrificing a complete view of 3d LCS in the turbulent channel. The extraction threshold
 372 was set to $s = 50000$, a compromise value between speed and cost of extraction and

373 continuity of the extracted surfaces. The FSLE fields were calculated for an interval of
374 1.5 time units with a time step of 0.1 units.

375 The 3d LCSs are rendered in figure 13, in a sequence of time instants, as they
376 pass through the calculation domain. They have a clearly 3d shape and move with the
377 flow. The LCS seem to create a boundary between the inner turbulent region and the
378 outer region that is practically devoid of FSLE. The highest LCS have δ -scale heights
379 above the wall, and have a distinct mushroom shape enclosing the regions of the channel
380 closer to the wall, where high FSLE values can be found. Near the wall, the LCS adopt
381 the shape of sheets parallel to it, which reflects the high rates of shear that occur in
382 that region. These sheets form the base of the mushroom-shaped excursions up to the
383 channel center.

384 4. Oceanic flow

385 Contrarily to the turbulent flow of the previous section, large scale oceanic flows,
386 naturally turbulent, can be considered as almost 2d due to rotation and stratification
387 effects. This fact makes the theory of 2d turbulence a very important tool to understand
388 the ocean processes that occur at large scales. The main characteristic of 2d turbulence
389 is the existence of an inverse energy cascade, from the small to the large scales and a
390 direct enstrophy cascade. These cascades manifests themselves by the creation of large
391 coherent vortices, and by the process of filamentation by which strain regions in the
392 boundaries of the vortices produce lines of vorticity that are continuously stretched and
393 deformed by the flow, concentrating the vorticity gradient in the small scales. This
394 behavior is often observed in oceanic flows thereby confirming the importance of the 2d
395 turbulent processes.

396 The results presented in this section were obtained in the Benguela ocean region,
397 situated off the west coast of southern Africa. It is characterized by a substantial
398 mesoscale activity in the form of eddies and filaments, and also by the northward drift
399 of Agulhas eddies. The velocity data set comes from a regional ocean model (ROMS)
400 simulation of the Benguela Region [53]. Additional details on this work can be found
401 in [37].

402 The three-dimensional FSLE fields were calculated for a 30 day period starting
403 September 17 of year 9, with snapshots taken every 2 days. The fields were calculated
404 for an area of the Benguela ocean region between latitudes 20°S and 30°S and longitudes
405 8°E to 16°E. The calculation domain extended vertically from 20 up to 580 m of depth.
406 Both backward and forward calculations were made in order to extract the attracting
407 and repelling LCS.

408 In the left panel of figure 14 a snapshot of the attracting LCSs for day 1 of the
409 calculation period is shown. The structures appear as thin vertical curtains, most of
410 them extending throughout the whole depth of the calculation domain. The horizontal
411 slices of the FSLE field in figure 14 (left panel) show that the attracting LCS fall on the

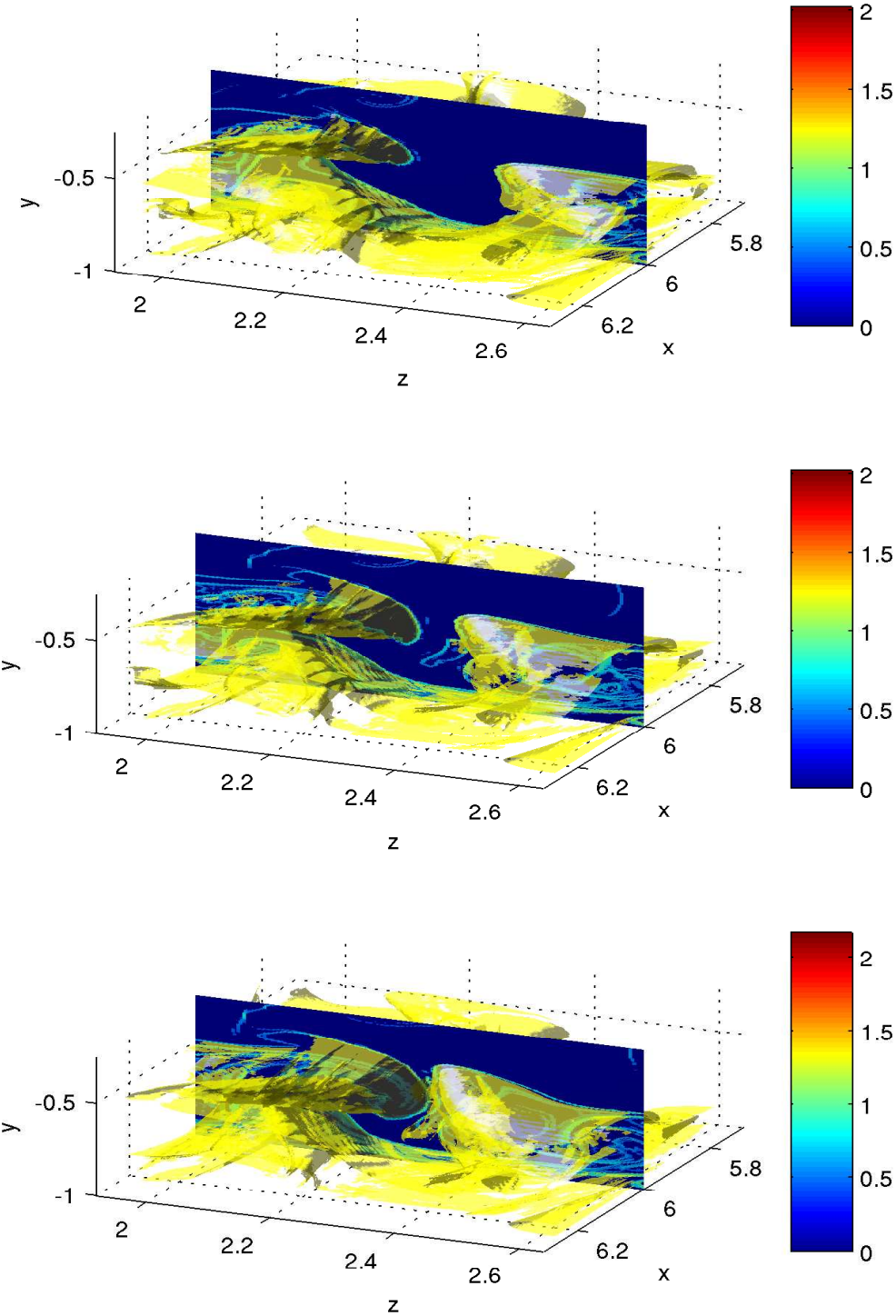


Figure 13. 3d attracting LCS in the channel flow together with a FSLE map at the fixed plane $x = 6.0$ ($x^+ = 1034$). Time goes from top to bottom, at intervals of 0.1 time units. The flow direction is in the positive x direction in each panel, and a wall is at the bottom. The sequence shows how one of the flow structures is advected and passes through the $x = 6.0$ plane.

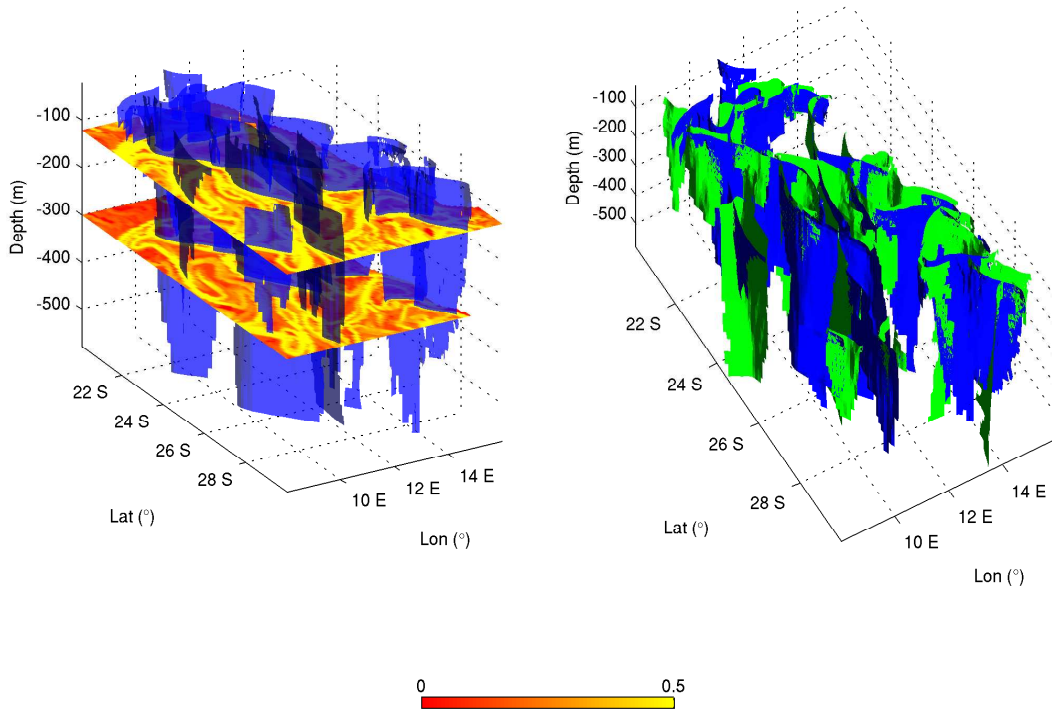


Figure 14. 3d LCS in the Benguela region for day 1 of the calculation period. Left panel (from [37]): Attracting LCS together with horizontal slices of the backward FSLE field at 120 m and 300 m depth. Right panel: Attracting (blue) and repelling (green) LCS. Colorbar refers to colormap of horizontal slices in the left panel. The units of the colorbar are day^{-1} .

412 maximum FSLE field lines, as in the case of the turbulent channel flow (figure 13). The
 413 FSLE fields themselves exhibit a variation in intensity that decreases with depth, although
 414 a local maximum is found at ~ 100 m (not shown). The ridges also seem to be weaker
 415 as the depth increases since for the same strength threshold, the extracted portions of
 416 the ridges become less extent and eventually vanish. The attracting and repelling LCS
 417 (figure 14, right panel) populate the calculation region, testifying the enhanced mixing
 418 activity that is known to occur in that particular ocean region. The quite entangled
 419 “web” in which attracting and repelling LCSs intersect mutually provides the skeleton
 420 for the barriers and pathways controlling transport [6, 11].

421 At this point, it may help to stress the differences between the Eulerian and
 422 Lagrangian detection of coherent structures. This can be seen in figure 15 where the
 423 boundaries of a mesoscale eddy are shown using the Q-criterion and the attracting and
 424 repelling LCS. The Q-criterion [54] uses the second invariant of $\nabla\mathbf{u}$:

$$425 \quad Q = \frac{1}{2}(\|\mathbf{\Omega}\|^2 - \|\mathbf{S}\|^2), \quad (12)$$

426 where $\|\mathbf{\Omega}\|^2 = \text{tr}(\mathbf{\Omega}\mathbf{\Omega}^T)$, $\|\mathbf{S}\|^2 = \text{tr}(\mathbf{S}\mathbf{S}^T)$, and $\mathbf{\Omega}$, \mathbf{S} are the antisymmetric and

427 symmetric components of $\nabla \mathbf{u}$, to identify regions where rotation dominates strain
 428 ($Q > 0$), commonly identified with coherent vortices, and strain dominated regions
 429 ($Q < 0$). We refer the reader to [55] and [56] for reviews and criticism of several
 430 Eulerian criteria.

431 Eulerian and Lagrangian measures limit approximately the same region, but are
 432 substantially different. The Q-criterion is related to the instantaneous configuration of
 433 the second invariant of $\nabla \mathbf{u}$ and therefore conveys only local information about fluid flow
 434 processes. The Lagrangian perspective, on the other hand, provides an integration of
 435 the temporal evolution of material properties of the flow, e.g. material transport, and
 436 thus should give more meaningful information about the processes that rely on ocean
 437 material transport.

438 This issue can be further explored by looking at a filamentation event (described
 439 more extensively in [37]). A set of particles were released inside the eddy at day 1
 440 at a depth of 50 m. At day 11 of the calculation period (see figure 15), they have
 441 formed a filament that is expelled from the eddy, so that particles clearly cross the Q-
 442 criterion isosurface. This shows that the Eulerian criteria is inadequate as an indicator
 443 of regions of material transport in the flow. On the contrary, it can be observed that
 444 the Lagrangian description of the eddy boundaries does bear relation with material
 445 transport into and out of the eddy, since the particle filament leaves the enclosed region
 446 that we associate with the mesoscale eddy by following one of the identified Lagrangian
 447 boundaries.

448 5. Conclusions

449 Lyapunov exponents are useful to identify Lagrangian coherent structures in turbulent
 450 flows. These constitute the pattern determining the pathways of particle transport in
 451 the flow and thus strongly influence the transport and mixing properties in the fluid.

452 In this paper we have used a particular type of Lyapunov exponents, the so-called
 453 Finite-Size Lyapunov exponents, to identify LCS in 3d flows. The finite size Lyapunov
 454 exponent was used to measure the rate of stretching of initially nearby fluid particles
 455 in the flow domain and the Lagrangian coherent structures were identified as the the
 456 ridges of the FSLE field. These ridges were filtered in order to retain only the strongest
 457 attracting or repelling structures.

458 In a turbulent channel flow, the FSLE field is organized into longitudinal structures
 459 close to the wall that develop into sloping ones away from the wall. Correlations in the
 460 streamwise and spanwise direction show the typical dimensions of these structures. They
 461 were found to be similar to the Eulerian coherent structures that are known to exist in
 462 this same regions of the turbulent channel. Specially, elongated streamwise vortices that
 463 move low speed fluid away from the wall into the channel core. In 3d, the LCSs appear
 464 as mushroom-shaped excursions of near-wall sheet-like structures of a scale comparable
 465 to the channel width. They separate the channel into an interior region, where the FSLE
 466 attains high values, and an exterior region, showing low FSLE values. The distribution

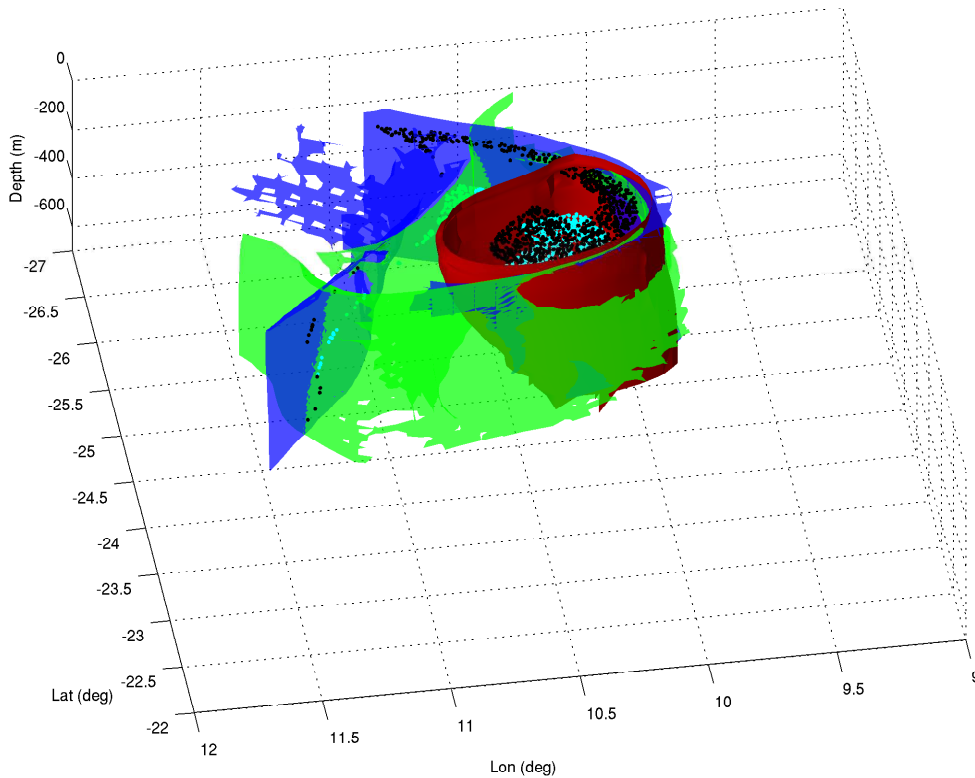


Figure 15. Attracting (blue) and repelling (green) LCS on day 11 of the calculation period together with Q-criterion isosurface at $Q = 10^{-10}$ (red). The particles (black dots) were released inside the eddy at day 1 at a depth of 50 m and are leaving now the eddy as a filament along the upper part of the attracting LCS.

467 of LCS in the turbulent channel resembles the commonly accepted picture where upward
 468 excursions of near wall fluid coexist with inward rushes of mid-channel irrotational flow.
 469 Further work is necessary to elucidate the relations between LCS and fluid transport in
 470 these type of flows, not least because the visualization of 3d structures and transport in
 471 turbulence is a complex and time-consuming subject.

472 In a quasi-2d mesoscale oceanic flow, the LCSs appear as quasi-vertical surfaces
 473 highlighting the fact that dispersion in this case is mainly horizontal. The high mixing
 474 activity can be deduced from the proliferation of LCS in the flow domain and their
 475 mutual intersection. These LCS were seen to provide barriers and pathways to transport
 476 in the case of a mesoscale eddy, contrary to Eulerian measures that failed to provide
 477 indicative locations or directions of major transport events.

478 The main difference between these two 3d turbulent flows with respect to the LCSs
 479 seems to be the fact that in the case of oceanic flow, turbulence was limited to the
 480 horizontal plane whereas in the channel flow case, turbulent fluctuations in all three space
 481 directions had similar magnitude, thereby producing much more complex 3d shapes in
 482 this latter case. In the oceanic flow, vertical motions have a tendency to be suppressed
 483 by the combined effects of the Earth's rotation and the stratification of the ocean. This

484 results in the aforementioned dominance of horizontal dispersion. The quasi-horizontal
 485 character of oceanic flows results in a phenomenology of turbulence similar to that of
 486 2d turbulence rather than to 3d turbulence.

487 We note that there are fundamental differences between the Lagrangian and
 488 Eulerian coherent structures, although they can actually have a common interpretation
 489 as vortices or shear layers. Lagrangian coherent structures have a clear impact in particle
 490 trajectories whereas Eulerian coherent structures are related to space/time coherency
 491 in, e.g., velocity signals and do not necessarily affect particles. In the above comparison,
 492 only the strongest FSLE features had a clear connection to the features in the Eulerian
 493 distribution, which indicates that, inversely, only the Eulerian features that live long
 494 enough or are strong enough to affect particles in a discernible fashion will appear in
 495 the Lagrangian point of view of coherent structures.

496 The results shown in this paper highlight the usefulness of Lyapunov analysis and
 497 dynamical systems theory as a tool to study transport and mixing in fluid flows, through
 498 the concept of Lagrangian coherent structures.

499 Acknowledgements

500 This work was supported by Ministerio de Economía y Competitividad (Spain) and
 501 Fondo Europeo de Desarrollo Regional through project FISICOS (FIS2007-60327). JHB
 502 acknowledges financial support of the Portuguese FCT (Foundation for Science and
 503 Technology) and Fundo Social Europeu (FSE/QREN/POPH) through the predoctoral
 504 grant SFRH/BD/63840/2009.

505 References

- 506 [1] Artale V, Boffetta G, Celani A, Cencini M and Vulpiani A 1997 *Phys. Fluids* **9** 3162–3171
 507 [2] Aurell E, Boffetta G, Crisanti A, Paladin G and Vulpiani A 1997 *J. Phys. A* **30** 1–26
 508 [3] Boffetta G, Lacorata G, Redaelli G and Vulpiani A 2001 *Physica D* **159** 58–70
 509 [4] Lapeyre G 2002 *Chaos* **12**(3) 688–698
 510 [5] Boffetta G, Celani A, Cencini A, Lacorata G and Vulpiani A 2000 *Chaos* **10** 50–60
 511 [6] d’Ovidio F, Fernández V, Hernández-García E and López C 2004 *Geophys. Res. Lett.* **31** L17203
 512 [7] Poje A C, Haza A C, Özgökmen T M, Magaldi M G and Garraffo Z D 2010 *Ocean Modell.* **31**
 513 36–50
 514 [8] Haller G 2000 *Chaos* **10**(1) 99–108
 515 [9] Haller G and Yuan G 2000 *Physica D* **147** 352–370
 516 [10] Joseph B and Legras B 2002 *J. Atm. Sci.* **59** 1198–1212
 517 [11] Mancho A M, Small D and Wiggins S 2006 *Phys. Rep.* **437** 55–124
 518 [12] d’Ovidio F, Isern J, López C, Hernández-García E and García-Ladona E 2009 *Deep-Sea Res. I* **56**
 519 15–31
 520 [13] Peacock T and Dabiri J 2010 *Chaos* **20** 017501 (pages 3)
 521 [14] Shadden S C, Lekien F and Marsden J E 2005 *Physica D*. **212** 271–304
 522 [15] Lekien F, Shadden S C and Marsden J E 2007 *J. Math. Phys.* **48** 065404
 523 [16] Haller G 2011 *Physica D* **240** 574–598
 524 [17] Haller G and Beron-Vera F J 2012 *Physica D* **241** 1680–1702
 525 [18] Hernandez-Carrasco I, López C, Hernández-García E and Turiel A 2011 *Ocean Modell.* **36** 208–218

- [19] Molcard A, Poje A and Özgökmen T 2006 *Ocean Modell.* **12** 268–289
- [20] Branicki M and Wiggins S 2010 *Nonlinear Processes Geophys* **17** 1–36
- [21] du Toit P and Marsden J 2010 *J. Fixed Point Theory Appl.* **7**(2) 351–384
- [22] Tang W, Chan P W and Haller G 2011 *Journal of Applied Meteorology and Climatology* **50** 325–338
- [23] Tallapragada P, Ross S D and Schmale III D G 2011 *Chaos* **21** 033122 ISSN 10541500
- [24] Green M A, Rowley C W and Haller G 2007 *J. Fluid Mech.* **572** 111–120
- [25] Haller G 2001 *Physica D* **149** 248–277
- [26] Bakun A 1996 *Patterns in the ocean. Ocean processes and marine population dynamics* (California Sea Grant College System, NOAA and Centro de Investigaciones Biológicas del Noroeste, La Paz, BCS Mxico)
- [27] Garçon V, Oschlies A, Doney S, McGillicuddy D and Waniek J 2001 *Deep Sea Research Part II: Topical Studies in Oceanography* **48** 2199–2226
- [28] Lévy M, Klein P and Treguier A 2001 *Journal of Marine Research* **59** 535–565
- [29] Lévy M 2008 *Lecture Notes in Physics* **744** 219–261
- [30] Rossi V, López C, Sudre J, Hernández-García E and Garçon V 2008 *Geophys. Res. Lett.* **35** L11602
- [31] Rossi V, López C, Hernández-García E, Sudre J, Garçon V and Morel Y 2009 *Nonlinear Processes Geophys* **16** 557–568
- [32] Tew Kai E, Rossi V, Sudre J, Weimerskirch H, López C, Hernández-García E, Marsac F and Garçon V 2009 *Proc. Natl. Acad. Sci. U.S.A.* **106** 8245–8250
- [33] Olascoaga M 2010 *Nonlinear processes in geophysics* **17** 685
- [34] Branicki M and Malek-Madani R 2010 *Nonlinear Processes in Geophysics* **17** 149–168
- [35] Branicki M, Mancho A M and Wiggins S 2011 *Physica D* **240** 282 – 304
- [36] Özgökmen T M, Poje A C, Fischer P F and Haza A C 2011 *Ocean Modell.* **39** 311–331
- [37] Bettencourt J, López C and Hernández-García E 2012 *Ocean Modell.* **51** 73–83
- [38] Beron-Vera F, Olascoaga M J, Brown M G, Koçak H and Rypina I I 2010 *Chaos* **20** 017514
- [39] Pouransari Z, Speetjens M and Clercx H 2010 *J. Fluid Mech.* **654** 5–34
- [40] Schultz T, Theisel H and Seidel H P 2010 *IEEE Transactions on Visualization and Computer Graphics* **16** 109–119
- [41] Eberly D, Gardner R, Morse B, Pizer S and Scharlach C 1994 *Journal of Mathematical Imaging and Vision* **4** 353–373
- [42] Sadlo F and Peikert R 2007 *IEEE Transactions on Visualization and Computer Graphics* **13** 1456–1463
- [43] Tennekes H and Lumley J L 1972 *A First Course in Turbulence* (The MIT Press)
- [44] Robinson S K 1991 *Annu. Rev. Fluid Mech.* **23** 601–639
- [45] Holmes J, Lumley J L and Berkooz G 1998 *Turbulence, Coherent Structures, Dynamical Systems and Symmetry* Cambridge Monographs on Mechanics (Cambridge University Press)
- [46] Pan C, Wang J and Zang C 2009 *Science in China Series G: Physics, Mechanics & Astronomy* **52** 248–257
- [47] Adrian R J 2007 *Phys. Fluids* **19** 041301
- [48] Moser R D, Kim J and Mansour N N 1999 *Phys. Fluids* **11** 943–945
- [49] Gibson J F 2012 *Channelflow: A spectral Navier-Stokes simulator in C++* Tech. rep. U. New Hampshire
- [50] Kim J, Moin P and Moser R 1987 *Journal of Fluid Mechanics* **177** 133–166
- [51] Jeong J, Hussain F, Schoppa W and Kim J 1997 *Journal of Fluid Mechanics* **332** 185–214
- [52] John Kim and Fazole Hussain 1993 *Physics of Fluids* **5** 695–706
- [53] Le Vu B, Gutknecht E, Machu E, Dadou I, Veitch J, Sudre J, Paulmier A and Garçon V 2011 *submitted to JMR*
- [54] Hunt J C R, Wray A A and Moin P 1988 *Eddies, streams and convergence zones in turbulent flows* Tech. Rep. CTR-S88 Center for Turbulence Research, Standford University 193–208
- [55] Jeong J and Hussain F 1995 *J. Fluid Mech.* **285** 69–94
- [56] Haller G 2005 *J. Fluid Mech.* **525** 1–26